nature materials

ARTICLES

https://doi.org/10.1038/s41563-019-0514-1

Kinetic pathways of crystallization at the nanoscale

Zihao Ou[1,10], Ziwei Wang[2,10], Binbin Luo[1], Erik Luijten[3,4,5,6*] and Qian Chen[1,7,8,9*]

Nucleation and growth are universally important in systems from the atomic to the micrometre scale as they dictate structural and functional attributes of crystals. However, at the nanoscale, the pathways towards crystallization have been largely unexplored owing to the challenge of resolving the motion of individual building blocks in a liquid medium. Here we address this gap by directly imaging the full transition of dispersed gold nanoprisms to a superlattice at the single-particle level. We utilize liquid-phase transmission electron microscopy at low dose rates to control nanoparticle interactions without affecting their motions. Combining particle tracking with Monte Carlo simulations, we reveal that positional ordering of the superlattice emerges from orientational disorder. This method allows us to measure parameters such as line tension and phase coordinates, charting the nonclassical nucleation pathway involving a dense, amorphous intermediate. We demonstrate the versatility of our approach via crystallization of different nanoparticles, pointing the way to more general applications.

The physical properties of crystals, such as structure, shape, defects, domain size and polymorphism, display a wide variability, strongly correlated with the crystallization pathways underlying their formation[1–3], with ramifications for mineralization[4], pharmaceuticals[5], optics[6] and electronics[7]. For example, carbonate-silica minerals can be engineered into diversely shaped device elements (for example, vase, stem or coral) by dynamically sculpting the curved nuclei that arise in accretive crystallization[8]. Protein crystallization can be accelerated by orders of magnitude via critical density fluctuations, allowing the creation of high-quality lattices for structural analysis and drug formulation[9]. DNA-coated micrometre-sized colloids can be grown into cubic diamond lattices with an omnidirectional photonic bandgap by starting from preformed seeds with tetrahedral symmetry[10]. The central role of crystallization in creating building blocks spanning this range of length scales makes understanding and engineering the underlying pathways of fundamental interest and crucially relevant for applications.

Due to the stochastic nature of nucleation and growth, an effective route to mechanistic understanding is to directly capture the translational and rotational motion of individual building blocks as they interact and crystallize. On the micron scale, this approach has revealed a series of crystallization pathways beyond classical nucleation theory, such as prenucleation cluster formation[11], multi-step nucleation[12] and diffusion-limited solidification[13], via time-lapse optical microscopy. For nanoscale entities, a richer variety of phases has been observed, such as quasi-[14], hierarchical[15] and clathrate crystals[16]. The pathways of these crystals can be more complicated, owing to the increased importance of discreteness and fluctuations resulting from the fact that the building blocks and solvent and ligand molecules have comparable length scales[17]. However, direct imaging of dynamics at the nanoscale has been challenging, because transmission electron microscopy (TEM) with the needed spatial resolution[18] has not been compatible with the liquid media in which crystallites nucleate and grow.

Here we exploit recent advances in low-dose liquid-phase TEM, a technique rapidly gaining importance in materials research[2,19–22], to achieve the in situ imaging of nanoscale entities ordering into crystals, distinct from the non-periodic nanoparticle aggregates observed in recent liquid-phase TEM studies[21,23]. We employ a sandwich geometry of two SiN_x chips accommodating and sealing, against the high vacuum of TEM, a liquid suspension containing many interacting nano-entities (Methods and Fig. 1a). We focus on a system of triangular gold nanoprisms as representative non-spherical, anisotropic nanoscale building blocks. The nanoparticle interactions are highly directional due to the large aspect ratio (100.5 ± 9.5 nm side length, 7.5 nm thickness; Supplementary Note 1, Supplementary Fig. 1). Moreover, the prisms are coated with negatively charged thiolated ligands to render them well dispersed by electrostatic repulsion in the initial suspension (Fig. 1a).

We observe a surprising transition from dispersed prisms to a hexagonal lattice, which is constructed hierarchically in three dimensions (3D) from standing columns of stacked, misaligned prisms (solid arrowed path in Fig. 1a–c, Supplementary Note 2, Supplementary Video 1). The hierarchical construction proceeds as follows. Through radiolysis of water, the imaging beam monotonically increases the ionic strength in the illuminated region within seconds, facilitating counterion screening of the electrostatic repulsions (Supplementary Fig. 4)[22,23]. The dispersed prisms in this region thus experience a stronger net attraction than they do elsewhere, initiating stacking on the flat SiN_x chip into vertically standing columns (Supplementary Figs. 5, 20, 24, Supplementary Note 12, Supplementary Video 2). The prisms in a column are not in perfect registry but misaligned in an angular orientation (cf. circular projection in Fig. 1d–g, Supplementary Figs. 5, 6, Supplementary Table 3, Supplementary Note 3). These columns then interact to form the final structure, which appears as a hexagonal lattice of evenly spaced, dark, circular discs under TEM (Fig. 1b, Supplementary Videos 1, 3). The equilibrium lattice constant measured from the TEM images matches that for hexagonally packed columns with touching edges (Supplementary Fig. 8). Voronoi cell analysis of the movies shows that the columns vibrate rapidly, eventually annealing all imperfectly bonded 5- and 7-fold clusters into hexagonal sublattice units

[1]Department of Materials Science and Engineering, University of Illinois, Urbana, IL, USA. [2]Graduate Program in Applied Physics, Northwestern University, Evanston, IL, USA. [3]Department of Materials Science and Engineering, Northwestern University, Evanston, IL, USA. [4]Department of Engineering Sciences and Applied Mathematics, Northwestern University, Evanston, IL, USA. [5]Department of Chemistry, Northwestern University, Evanston, IL, USA. [6]Department of Physics and Astronomy, Northwestern University, Evanston, IL, USA. [7]Department of Chemistry, University of Illinois, Urbana, IL, USA. [8]Materials Research Laboratory, University of Illinois, Urbana, IL, USA. [9]Beckman Institute for Advanced Science and Technology, University of Illinois, Urbana, IL, USA. [10]These authors contributed equally: Zihao Ou, Ziwei Wang. *e-mail: luijten@northwestern.edu; qchen20@illinois.edu

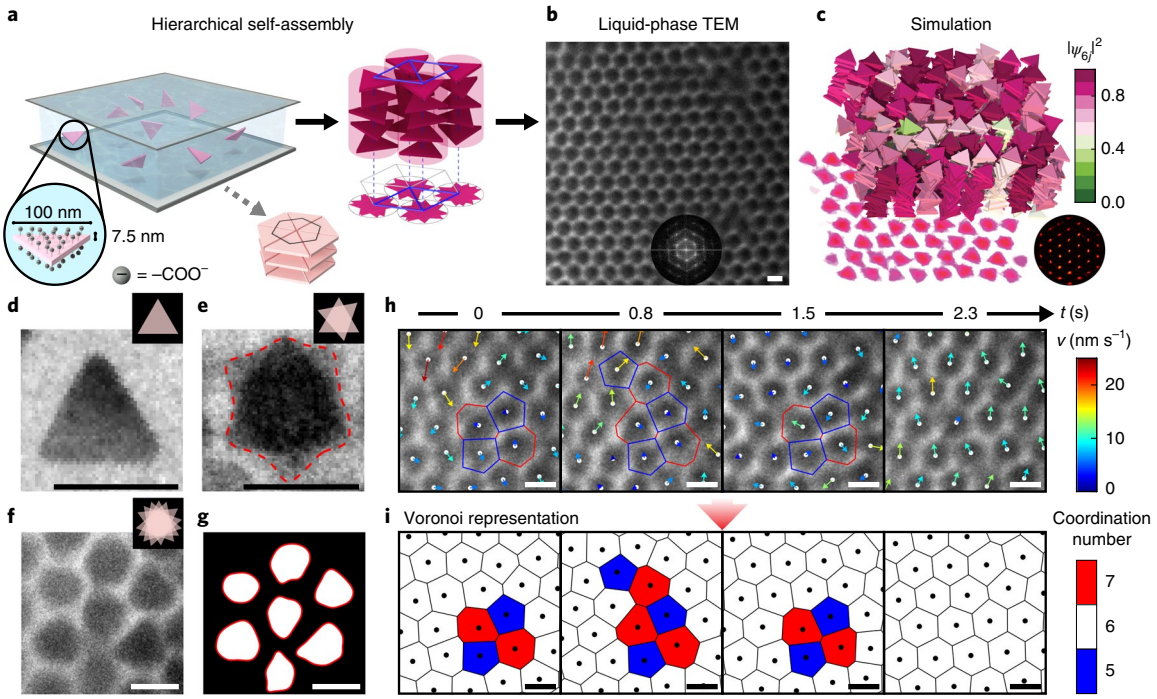

Fig. 1 | Gold triangular nanoprisms crystallize hierarchically in 3D to an unexpected hexagonal lattice. a–c, Illustration of the hierarchical crystallization process. **a**, An aqueous suspension of nanoprisms sealed and sandwiched between two SiN_x chips. Instead of packing into a space-filling honeycomb lattice (dotted arrow), the nanoprisms stack face-to-face into columns (magenta), which subsequently bundle into a hexagonal lattice (solid arrow). **b**, Liquid-phase TEM image showing the highly ordered hexagonal lattice. Inset shows the Fourier transform of the image. **c**, MC simulations confirm the hexagonal lattice as the thermodynamically stable structure, as illustrated via a colour map denoting the squared modulus of the bond orientational order parameter[27] per column j, $|\psi_{6j}|^2$, two-dimensional (2D) projection and diffraction pattern. **d–g**, Liquid-phase TEM snapshots showing the stacking of misaligned prisms in top view: an individual prism sitting on the SiN_x chip (**d**), two prisms stacking with misalignment (**e**, polygonal projection contoured in dotted red line) and more prisms stacking into columns (**f**,**g**, nearly circular projections contoured in solid red lines in the binary image). **h**,**i**, Time-lapse liquid-phase TEM images (**h**) and corresponding Voronoi representations (**i**) of the lattice, showing the annealing of imperfectly coordinated sites. Colour of each cell denotes the coordination number. Arrows in the top panel are coloured by the magnitude of the instantaneous velocity of individual columns v calculated from successive TEM images. Scale bars for all images: 100 nm.

(Fig. 1h,i, Supplementary Fig. 3, Supplementary Table 1). At the low electron dose rates used here (3.7–8.9 e^- Å^{-2} s^{-1}), the ligands on the prism surface remain intact, and nanoparticle interactions are not affected other than through variation of the ionic strength[23] (Supplementary Fig. 4, Supplementary Table 2, Supplementary Notes 4, 5). Quantification of the relationship between dose rate and ionic strength makes it possible to trigger and capture the complete crystallization starting from dispersed prisms.

The hierarchical hexagonal lattice differs from the space-filling honeycomb lattice predicted by prior computer simulations (dotted arrowed path, Fig. 1a)[24], because the nanoparticles in our experiments are not 'hard-core' geometric shapes, but interact via a combination of van der Waals and electrostatic interactions. The hierarchical lattice also transcends the simple one-dimensional columns formed from face-to-face prism stacking[25] or other loosely packed chain-like aggregates observed in liquid-phase TEM[21,23], where substrate adhesion prevents nanoparticle motions in 3D. Repeatedly switching the electron beam off and on leads to reversible crystallization and disassembly of the hexagonal lattice, confirming the role of local ionic strength variations (Supplementary Video 4).

Explicit calculation shows that the misaligned stacking of prisms into columns originates from an intricate balance between pairwise interaction energy and rotational entropy. The comparable size of the building blocks and the interaction range necessitate far more detailed modelling than the 'hard' excluded-volume potentials[24] typically employed for anisotropic colloids, so we compute the inter-prism pairwise interaction $E_{tot} = E_{vdW} + E_{el}$ (with E_{vdW} the van der Waals attraction and E_{el} the electrostatic repulsion) via numerical summation over 250,000 discretized elements per prism (Supplementary Note 8). The net interaction E_{tot} is highly directional and strongly attractive, explaining why the prisms predominantly stack in parallel and coaxially, with minimal tilting of their basal planes at a vertical separation d (Supplementary Fig. 15). To understand the energetics of prism misalignment, we plot the computed pairwise interactions in polar maps along relative orientation $\Delta\theta$, the spin-angle difference between neighbouring prisms (Fig. 2a). At the effective experimental ionic strength, E_{el} favours anti-alignment of adjacent prisms, while the alignment-favouring E_{vdW} dominates slightly, resulting in a minimum in interaction energy E_{tot} at $\Delta\theta = 0$ and vertical separation d_{min} (Fig. 2b). Yet, E_{el} suppresses variation of E_{tot} near $\Delta\theta = 0$, so that rotational entropy negates the energetic penalty for small misalignments (penalty less than k_BT for $|\Delta\theta| < \pi/10$; Fig. 2c), consistent with the experimental observations (Fig. 1d–g).

The misalignment of prisms within each column has consequences that propagate to the large-scale crystal structure, giving rise to radially isotropic interactions between columns that promote their hexagonal packing. From the explicit pairwise interaction E_{tot} we obtain an effective functional form (Supplementary Figs. 16–19, Supplementary Notes 9, 10) that allows efficient large-scale Monte Carlo (MC) simulations (Supplementary Note 11). On the

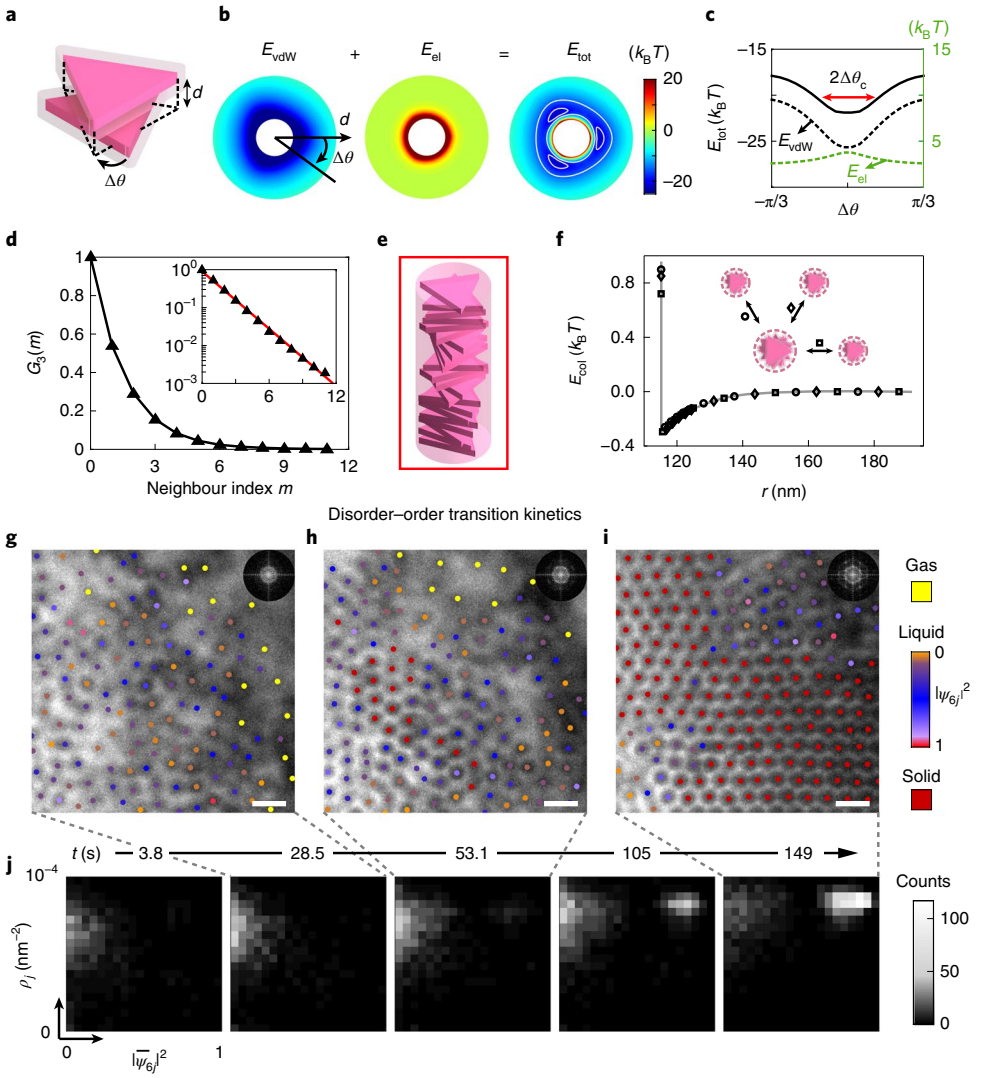

Fig. 2 | Energetics and in situ observation of the crystallization process. a–c, Pairwise interaction between two stacked prisms at the effective experimental ionic strength of 0.5 M. **a**, Definitions of vertical separation d and spin-angle difference $\Delta\theta$. **b**, Coloured polar maps showing van der Waals attraction E_{vdW}, electrostatic repulsion E_{el} and total interaction energy $E_{tot} = E_{vdW} + E_{el}$ as a function of d and $\Delta\theta$. **c**, Pairwise energies versus $\Delta\theta$ at $d = d_{min}$, the prism separation at the global energy minimum. $[-\Delta\theta_c, \Delta\theta_c]$ marks the spin-angle range with an energy penalty less than k_BT. **d**, Orientational pair correlation function between prisms in a single column, $G_3(m) = \langle \cos[3(\theta_i - \theta_{i+m})] \rangle_i$, computed from simulations. Inset: $G_3(m)$ on a semi-logarithmic scale, with a fitted decay length of 1.86 prisms, indicating low orientational correlation beyond the second neighbour. **e**, Representative snapshot of a column. **f**, Inter-column interaction E_{col} is independent of relative orientation (marked by different symbols). **g–i**, Time-lapse TEM images show the real-time crystallization process, with 'gas' columns coloured yellow, 'liquid' columns coloured according to $|\psi_{6j}|^2$ and 'solid' columns coloured red. Insets: Fourier transforms highlighting the increasing crystalline order. **j**, Corresponding order-density ($|\bar{\psi}_{6j}|^2, \rho_j$) histograms showing the counts of columns exhibiting specific $|\bar{\psi}_{6j}|^2$ and ρ_j values. The liquid domain (low $|\bar{\psi}_{6j}|^2$) gradually expands and transitions to the solid domain (high $|\bar{\psi}_{6j}|^2$) at approximately constant ρ_j. Scale bars: 200 nm.

individual column level, the misalignment between adjacent prisms propagates as the prism number M in a column increases (Supplementary Figs. 23, 27). For a typical M of 23, we find that the orientational correlation function along the column axis decreases exponentially to less than 10% for the fourth neighbour, reflecting high orientational randomness (Fig. 2d,e, Supplementary Video 5, Supplementary Fig. 26). As a result, the inter-column interactions at different relative column orientations collapse onto a master curve (Fig. 2f). The potential well of this curve is shallow ($-0.3\,k_BT$), making columns interact as nearly 'hard' circular cylinders. Thermodynamically, such cylinders are expected to crystallize at sufficiently high volume fractions[26], consistent with our experiments and MC simulations (Fig. 1b,c, Supplementary Video 3). Note that inter-column interactions in turn affect the intra-column alignment (Supplementary Fig. 28, Supplementary Note 13.5); this is fully taken into account in the large-scale simulations.

Since the agreement of the multiscale computation and the TEM observations underpins the thermodynamic origin of the observed hierarchical crystallization, we develop and apply single-particle tracking codes to the TEM movies, obtaining a series of otherwise elusive parameters quantifying the crystallization pathway. Accurate statistics are achieved by locating more than 110,000 columns in three independent movies (Supplementary Note 6, Supplementary Fig. 7, Supplementary Videos 1, 4, 6). To specify the crystalline nuclei, we measure the sixfold symmetry of bonds for each column j using the modulus squared bond-orientational order parameter[27] $|\psi_{6j}|^2$. The establishment of crystalline order is accompanied by density fluctuations, which we illustrate by directly

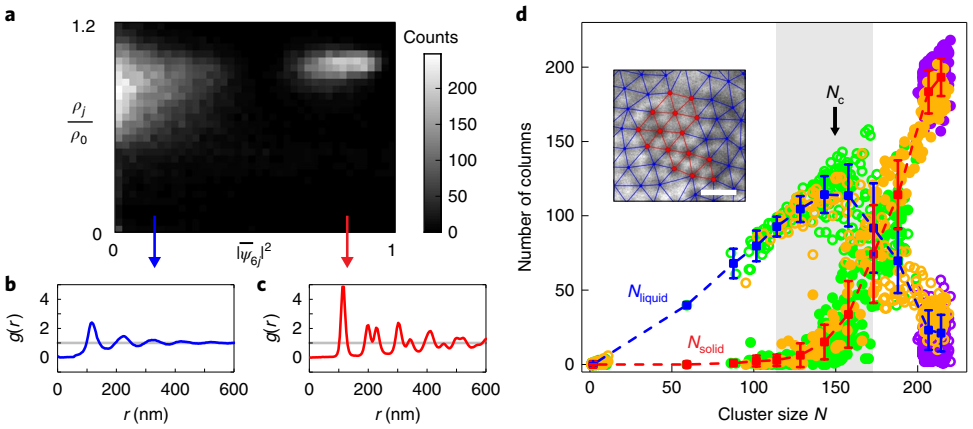

Fig. 3 | Multi-step crystallization of a nanoparticle superlattice via a dense, amorphous liquid state as the intermediate. a, Direct visualization of the crystallization pathway in the order-density $\left(|\bar{\psi}_{6j}|^2, \rho_j\right)$ histogram collected during the full crystallization process (Supplementary Video 6). The populated region on the left represents the liquid columns with low structural order, whereas the bright region on the right represents the ordered solid. **b**,**c**, Radial distribution functions corresponding to the two regions highlight their structural differences. **d**, Number of liquid columns N_{liquid} (open circles) and solid columns N_{solid} (filled circles) in a cluster of N columns. Data from three independent experiments (differentiated by colour) are described by master curves for liquid columns (blue, mean ± s.d. from three independent experiments) and solid columns (red, mean ± s.d. from three independent experiments). Grey shaded region highlights where the liquid–solid transition occurs, illustrated by the TEM image (inset, scale bar: 200 nm) showing an emerging solid nucleus (red) surrounded by a liquid network (blue). The master curves reveal a characteristic cluster size N_c beyond which a stable solid cluster emerges and continues to grow.

measuring the evolution of the local density ρ_j, the inverse Voronoi cell area[12], as local order develops (Supplementary Fig. 9). Jointly, these two instantaneous local parameters describe the structural state of a column at any given time. The time-lapse TEM images (Fig. 2g–i, Supplementary Fig. 11) show that initially the columns are in a dilute phase, translating rapidly—the analogue of a 'gas' state with low $|\psi_{6j}|^2$ and low ρ_j ($\rho_j < 0.5\rho_0$, where ρ_0 is the density of a dense-packed hexagonal lattice). Subsequently, a region of columns with low $|\psi_{6j}|^2$ but higher ρ_j appears and transiently coexists with the gas, analogous to a dense, amorphous 'liquid' state. This liquid region expands steadily until stable hexagonal crystallites nucleate from within, the 'solid' state (characterized by a solid bond number, the number of crystalline nearest neighbours of column j, $\xi_j \geq 4$, see Supplementary Fig. 9). The liquid columns envelop the nuclei as they grow into large crystalline domains, which represent the intermediate during the crystallization. Note that this observed liquid phase is indeed a metastable intermediate characteristic of a two-step crystallization process, rather than a transient state (further discussion in Supplementary Note 6.6). These insights into the prenucleation intermediate and its dynamic transformation into nuclei are enabled by observing time-dependent nanoscale motions and rearrangements at the single-particle level, which is not possible via common in situ techniques, such as small-angle X-ray scattering, that only resolve ensemble-level parameters (for example lattice spacing, symmetry group, domain size)[25,28].

To quantify the crystallization pathway, we illustrate the liquid-to-solid conversion in the plane of local order versus local density. We employ the coarse-grained order parameter[12] $|\bar{\psi}_{6j}|^2 = \left|\left(\sum_{k=0}^{Z^*} \psi_{6k}\right)/(Z^*+1)\right|^2$ to further distinguish the liquid and solid states, where the sum runs over column j and its Z^* nearest neighbours that belong to the same state (Supplementary Fig. 10). The time evolution of the $(|\bar{\psi}_{6j}|^2, \rho_j)$ histogram shows that the liquid domain expands along the $|\bar{\psi}_{6j}|^2$ axis, maintaining a high and roughly constant local density but significantly increasing the local order to reach the solid domain (Fig. 2j, Supplementary Video 6). The $(|\bar{\psi}_{6j}|^2, \rho_j)$ histogram accumulated over the full crystallization process (Fig. 3a) clearly distinguishes the intermediate state (left peak, liquid) and final lattice (right peak, solid), with corresponding radial distribution functions (Fig. 3b,c) resembling those of liquid and solid states of atomic matter. This nonclassical nucleation pathway involving formation of a dense amorphous intermediate was also found to assist crystallization from a dilute state in proteins[9,29] and Lennard-Jones systems[30], but hitherto could not be observed on the nanoscale.

The observed pathway is quantitatively consistent in independent experiments. For ease of comparison, we track the populations of liquid and solid columns in growing clusters, defined[12] as sets of contiguously bonded columns. Initially, the number of liquid columns N_{liquid} grows to a characteristic size N_c (Fig. 3d), consistent among multiple crystallization events, and then decreases steadily, while the number of solid columns N_{solid} grows at a higher rate until the cluster has fully solidified. This two-step process agrees with a phenomenological two-barrier free energy[30], where the intermediate liquid state acts as a 'wetting' layer that lowers the interfacial tension, so that ordering happens within (Fig. 3d, inset). Moreover, the short-range character of the inter-column interaction (Fig. 2f, with interaction range smaller than 25% of the column diameter) may be responsible for the existence of the liquid intermediate, consistent with previous theoretical work[9,30].

Taking this concept a step further quantitatively, we use statistical-mechanical principles[31] to determine the line tension from the cluster distribution for the gas–liquid interface from TEM movies. The result, $1.0 \pm 0.1\ k_BT$ per column diameter (Supplementary Fig. 12), is in remarkable agreement with the computed inter-column attraction of magnitude $0.9\ k_BT$ (three column pairs of $0.3\ k_BT$ each).

Lastly, full-scale MC simulations spanning the parameter space reveal how positional ordering is inextricably linked with orientational disorder (Methods, Supplementary Notes 9–11). To illustrate this 'order from disorder', we characterize the orientational order of prisms within a column via the triatic order parameter $S_\theta = \max_{\theta_0}\left\{\frac{1}{M}\sum_{i=1}^{M}\cos[3(\theta_i - \theta_0)]\right\}$ (ref. [32]), where θ_i denotes the in-plane spin angle of prism i in the column (Fig. 4a, free energy in Supplementary Fig. 25, Supplementary Note 13). We focus on 2D packing fractions $\phi_{2D} = N_{col}A_\Delta/(L_xL_y)$, where N_{col} is the total number of columns and A_Δ is the area of a prism face, between 0.362

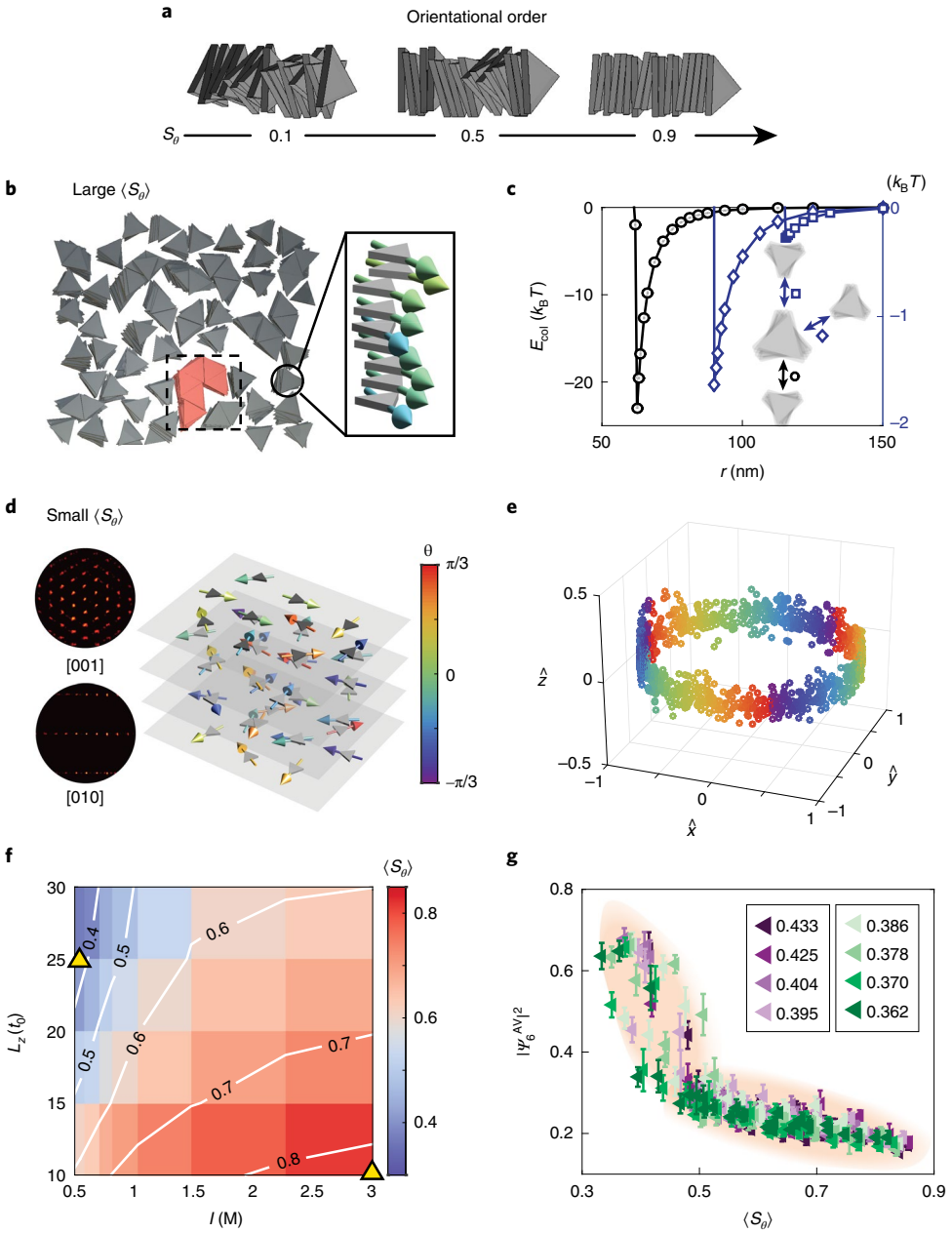

Fig. 4 | Positional ordering originates from orientational disorder. a, Orientational order S_θ of a column. **b**,**c**, Columns of highly aligned prisms aggregate into slowly evolving clusters (**b**), driven by strong and highly anisotropic inter-column interactions E_{col} (**c**), shown as a function of centre-to-centre distance r for three relative orientations: side-by-side (left axis, black circles), side-to-tip (right axis, blue rhombi) and tip-to-tip (right axis, blue squares). **d**, Orientationally highly disordered columns form a plastic crystal. Prism orientations are highlighted by arrows coloured according to their in-plane spin angle θ ($-\pi/3 < \theta < \pi/3$). Diffraction patterns confirm the positional columnar order. **e**, Orientational trajectory of an arbitrary prism reflects the orientational randomness in **d**. **f**, Column-averaged orientational order $\langle S_\theta \rangle$ as a function of ionic strength I and cell height L_z (in units of prism thickness t_0) at 2D packing fraction $\phi_{2D} = 0.386$. Yellow triangles mark the conditions for the highly orientationally ordered (right) and disordered (left) columns that give rise to the structures in panels **b** and **d**, respectively. **g**, Global hexagonal order, described by $|\Psi_6^{AV}|^2$ (mean ± standard error from 100 independent samples), develops over the 2D packing fraction range $0.362 < \phi_{2D} < 0.433$ as specified in the plot. Within this entire concentration range, data for widely different ionic strengths and cell heights collapse onto a master curve described by the global columnar order $\langle S_\theta \rangle$.

and 0.433, the regime where multiple phases can be realized. When columns are orientationally ordered (for example, $\langle S_\theta \rangle = 0.84$), the inter-column interaction exhibits a radial anisotropy and a deep attractive well for side-to-side columnar attachment ($-23\,k_BT$, Fig. 4b,c, Supplementary Video 7). The MC simulations reveal slowly evolving clusters of columns that are laterally connected. By contrast, on the same time scale, misaligned columns (for example $\langle S_\theta \rangle = 0.37$) fully crystallize into a perfect lattice (Fig. 4d,e, Supplementary Video 3). Systematically varying both cell height L_z and ionic strength I (Fig. 4f, Supplementary Table 4) at each 2D packing fraction ϕ_{2D}, we find a hexagonal lattice if $\langle S_\theta \rangle < 0.4$. The global hexagonal order parameter is a function solely of $\langle S_\theta \rangle$ for the entire ϕ_{2D} range, with data for a wide range of I and L_z collapsing onto a single master curve (Fig. 4g, see Supplementary Fig. 22 for different ϕ_{2D}).

This plastic mesophase, with simultaneous orientational randomness and positional ordering (Supplementary Figs. 20, 21), is akin to structures common in molecular solids[33], yet arises here without the conventional conditions of high axial symmetry and long-range repulsion[34]. The physical parameters measured for this model system of nanoprisms, involving both hierarchy and a high level of shape anisotropy, can provide experimental guidance to future refinements of theories for the pathways of nucleation and growth. To illustrate the versatility of our approach, we extend it to gold nanoparticles of different shapes, namely nanospheres and concave nanocubes (Supplementary Fig. 2, Supplementary Note 7). Capped with the same charged thiols as the nanoprisms, these nanoparticles are triggered to crystallize into high-quality 3D lattices following a similar mechanism (Supplementary Videos 8, 9, Supplementary Figs. 13, 14), validating the robustness of our low-dose liquid-phase TEM platform in probing nanoscale crystallization. As the approach is extended to other interacting nano-entities, more parameters can be derived from the imaged coordinates. Fluctuating local features (symmetry of nuclei, topological defects, strain map and so on) and global characteristics computable only from sufficient single-particle statistics (such as nucleation rate, phonon modes and nanoparticle interaction) are all of crucial importance for understanding the nanoscopic pathways of phase transitions. Our workflow, combining nanoscale-resolution imaging of particle motion and shape with a statistical-mechanical framework, can translate knowledge of fundamental interactions, fluctuations and motion on the nanoscale into free-energy landscapes and design rules that will make it possible to optimize dynamic switching of artificial[35] and biological[36] nanoscopic entities between different functional states.

Online content

Any methods, additional references, Nature Research reporting summaries, source data, extended data, supplementary information, acknowledgements, peer review information; details of author contributions and competing interests; and statements of data and code availability are available at https://doi.org/10.1038/s41563-019-0514-1.

Received: 5 September 2018; Accepted: 17 September 2019;
Published online: 28 October 2019

References

1. De Yoreo, J. J. et al. Crystallization by particle attachment in synthetic, biogenic, and geologic environments. *Science* **349**, aaa6760 (2015).
2. Loh, N. D. et al. Multistep nucleation of nanocrystals in aqueous solution. *Nat. Chem.* **9**, 77–82 (2017).
3. Li, B., Zhou, D. & Han, Y. Assembly and phase transitions of colloidal crystals. *Nat. Rev. Mater.* **1**, 15011 (2016).
4. Henzler, K. et al. Supersaturated calcium carbonate solutions are classical. *Sci. Adv.* **4**, eaao6283 (2018).
5. Chen, J., Sarma, B., Evans, J. M. B. & Myerson, A. S. Pharmaceutical crystallization. *Cryst. Growth Des.* **11**, 887–895 (2011).
6. John, S. Strong localization of photons in certain disordered dielectric superlattices. *Phys. Rev. Lett.* **58**, 2486–2489 (1987).
7. Choi, J.-H. et al. Exploiting the colloidal nanocrystal library to construct electronic devices. *Science* **352**, 205–208 (2016).
8. Noorduin, W. L., Grinthal, A., Mahadevan, L. & Aizenberg, J. Rationally designed complex, hierarchical microarchitectures. *Science* **340**, 832–837 (2013).
9. Ten Wolde, P. R. & Frenkel, D. Enhancement of protein crystal nucleation by critical density fluctuations. *Science* **277**, 1975–1978 (1997).
10. Ducrot, É., He, M., Yi, G.-R. & Pine, D. J. Colloidal alloys with preassembled clusters and spheres. *Nat. Mater.* **16**, 652–657 (2017).
11. Zhang, T. H. & Liu, X. Y. How does a transient amorphous precursor template crystallization. *J. Am. Chem. Soc.* **129**, 13520–13526 (2007).
12. Tan, P., Xu, N. & Xu, L. Visualizing kinetic pathways of homogeneous nucleation in colloidal crystallization. *Nat. Phys.* **10**, 73–79 (2013).
13. Kenneth, G. L. The physics of snow crystals. *Rep. Prog. Phys.* **68**, 855–895 (2005).
14. Ye, X. et al. Quasicrystalline nanocrystal superlattice with partial matching rules. *Nat. Mater.* **16**, 214–219 (2017).
15. Xia, Y. et al. Self-assembly of self-limiting monodisperse supraparticles from polydisperse nanoparticles. *Nat. Nanotechnol.* **6**, 580–587 (2011).
16. Lin, H. et al. Clathrate colloidal crystals. *Science* **355**, 931–935 (2017).
17. Batista, C. A., Larson, R. G. & Kotov, N. A. Nonadditivity of nanoparticle interactions. *Science* **350**, 1242477 (2015).
18. De Yoreo, J. J. & Sommerdijk, N. A. J. M. Investigating materials formation with liquid-phase and cryogenic TEM. *Nat. Rev. Mater.* **1**, 16035 (2016).
19. Park, J. et al. 3D structure of individual nanocrystals in solution by electron microscopy. *Science* **349**, 290–295 (2015).
20. Liao, H.-G., Cui, L., Whitelam, S. & Zheng, H. Real-time imaging of Pt_3Fe nanorod growth in solution. *Science* **336**, 1011–1014 (2012).
21. Sutter, E. et al. In situ microscopy of the self-assembly of branched nanocrystals in solution. *Nat. Commun.* **7**, 11213 (2016).
22. Schneider, N. M. et al. Electron–water interactions and implications for liquid cell electron microscopy. *J. Phys. Chem. C.* **118**, 22373–22382 (2014).
23. Kim, J., Ou, Z., Jones, M. R., Song, X. & Chen, Q. Imaging the polymerization of multivalent nanoparticles in solution. *Nat. Commun.* **8**, 761 (2017).
24. Agarwal, U. & Escobedo, F. A. Mesophase behaviour of polyhedral particles. *Nat. Mater.* **10**, 230–235 (2011).
25. Jones, M. R. et al. DNA-nanoparticle superlattices formed from anisotropic building blocks. *Nat. Mater.* **9**, 913–917 (2010).
26. Fraser, D. P., Zuckermann, M. J. & Mouritsen, O. G. Simulation technique for hard-disk models in two dimensions. *Phys. Rev. A* **42**, 3186–3195 (1990).
27. Savage, J. R., Blair, D. W., Levine, A. J., Guyer, R. A. & Dinsmore, A. D. Imaging the sublimation dynamics of colloidal crystallites. *Science* **314**, 795–798 (2006).
28. Liu, W. et al. Diamond family of nanoparticle superlattices. *Science* **351**, 582–586 (2016).
29. Sauter, A. et al. On the question of two-step nucleation in protein crystallization. *Faraday Discuss.* **179**, 41–58 (2015).
30. Lutsko, J. F. & Nicolis, G. Theoretical evidence for a dense fluid precursor to crystallization. *Phys. Rev. Lett.* **96**, 046102 (2006).
31. Auer, S. & Frenkel, D. Prediction of absolute crystal-nucleation rate in hard-sphere colloids. *Nature* **409**, 1020–1023 (2001).
32. Donev, A., Burton, J., Stillinger, F. H. & Torquato, S. Tetratic order in the phase behavior of a hard-rectangle system. *Phys. Rev. B* **73**, 054109 (2006).
33. Timmermans, J. Plastic crystals: a historical review. *J. Phys. Chem. Solids* **18**, 1–8 (1961).
34. Liu, B. et al. Switching plastic crystals of colloidal rods with electric fields. *Nat. Commun.* **5**, 3092 (2014).
35. Boles, M. A., Engel, M. & Talapin, D. V. Self-assembly of colloidal nanocrystals: from intricate structures to functional materials. *Chem. Rev.* **116**, 11220–11289 (2016).
36. Gruebele, M., Dave, K. & Sukenik, S. Globular protein folding in vitro and in vivo. *Annu. Rev. Biophys.* **45**, 233–251 (2016).

Methods

Chemicals. Sodium iodide (99.999%, NaI, Sigma-Aldrich), cetyltrimethylammonium bromide (CTAB) (BioXtra, ≥99%, $C_{19}H_{42}BrN$, Sigma-Aldrich), gold(III) chloride trihydrate (≥99.9%, $HAuCl4{\cdot}3H_2O$, Sigma-Aldrich), sodium citrate tribasic dihydrate (BioUltra, ≥99.5%, $HOC(COONa)(CH_2COONa)_2{\cdot}2H_2O$, Sigma-Aldrich), sodium borohydride (99%, $NaBH_4$, Sigma-Aldrich), L-ascorbic acid (BioXtra, ≥99.0%, $C_6H_8O_6$, Sigma-Aldrich), sodium hydroxide (99.99%, NaOH, Sigma-Aldrich), silver nitrate (≥99.0%, $AgNO_3$, Sigma-Aldrich), hexadecylpyridinium chloride monohydrate (CPC) (>98.0%, $C_{21}H_{38}ClN{\cdot}H_2O$, TCI), hydrochloric acid (99.999%, HCl, Alfa Aesar), sodium chloride (99.3%, NaCl, Fisher Scientific), sodium phosphate monobasic monohydrate (99.0–102.0%, $NaH_2PO_4{\cdot}H_2O$, EMD Millipore), sodium phosphate dibasic anhydrous (>99%, Na_2HPO_4, Acros) and 2-(2-[2-(11-mercapto-undecyloxy)-ethoxy]-ethoxy)-ethoxy-ethoxy-ethoxy-acetic acid (≥95%, $HS(CH_2)_{11}(OC_2H_4)_6OCH_2COOH$, Prochimia Surfaces) are purchased and used without further purification. All glassware is washed with aqua regia (mixture of HCl and HNO_3 with a volume ratio of 3:1), fully rinsed with water and dried before use. The water used in this work is nanopure water (18.2 MΩ cm at 25 °C) purified by a Milli-Q Advantage A10 system.

Gold nanoparticle synthesis, surface modification and liquid-phase TEM imaging. Triangular gold nanoprisms, gold nanospheres and gold concave nanocubes were synthesized based on published methods[23,25,37,38]. As-synthesized nanoparticles underwent a ligand-exchange process with carboxylate-terminated thiols ($HS(CH_2)_{11}(OC_2H_4)_6OCH_2COOH$) following a published method to render the surface negatively charged[23] (Supplementary Note 1).

The liquid-phase TEM imaging procedures were modified slightly for different nanoparticles. In a typical experiment, the nanoprisms were suspended in 34.5 mM pH = 8 phosphate-buffered saline solution. An aliquot of nanoparticle solution was transferred onto a SiN_x chip (window: 550 μm × 20 μm, 150 nm spacer flow echip, Protochips). The chip was assembled with another identical SiN_x chip in a Protochips Poseidon 210 liquid flow TEM holder. The liquid-phase imaging was carried out on a JEOL 2100 Cryo TEM with an LaB6 emitter at 200 kV, equipped with a Gatan Ultrascan charge-coupled device camera (Supplementary Note 2). Details of the imaging procedure as well as automated single-particle tracking and order-parameter analysis based on customized computer codes are provided in Supplementary Notes 3, 6.

Interaction calculations and computer simulations. To obtain the detailed pairwise interaction between prisms, a coarse-grained model was constructed in which the ligand-coated prisms were discretized as a mesh of beads with mesh spacing $\Delta_b = 0.5$ nm. The pairwise interaction between two arbitrarily oriented and positioned prisms was calculated by summing over all pairwise interactions between beads on the two prisms. Based on the coarse-grained model, an analytical model was derived for MC simulations, by approximating the pairwise interaction along different degrees of freedom with analytical functions that are computationally inexpensive to evaluate. To explore the phase space of the system, we performed large-scale MC simulations under different conditions in the canonical (*NVT*) ensemble of 576 to 1,472 prisms in a rectangular cell that was periodic along the *x* and *y* directions, but finite along the *z* direction (see Supplementary Table 4). Additional simulation and model details are provided in Supplementary Notes 8–13.

Data availability

The data that support the findings of this study are available from the corresponding authors upon request.

Code availability

Custom Matlab codes for image processing and particle tracking as well as the algorithms for the particle interactions and the MC simulations are available from the corresponding authors upon request.

References

37. Nikoobakht, B. & El-Sayed, M. A. Preparation and growth mechanism of gold nanorods (NRs) using seed-mediated growth method. *Chem. Mater.* **15**, 1957–1962 (2003).
38. O'Brien, M. N., Jones, M. R., Brown, K. A. & Mirkin, C. A. Universal noble metal nanoparticle seeds realized through iterative reductive growth and oxidative dissolution reactions. *J. Am. Chem. Soc.* **136**, 7603–7606 (2014).

Acknowledgements

The experiments and analysis of the experimental data presented in this research were supported by the US Department of Energy, Office of Basic Energy Sciences, Division of Materials Sciences and Engineering under award no. DE-FG02-07ER46471 through the Materials Research Laboratory at the University of Illinois (the nanoprism system) and the National Science Foundation through award no. DMR-1752517 (the concave nanocube and nanosphere systems). The theoretical model and simulations presented in this research were supported by the National Science Foundation through award no. DMR-1610796 and based upon work supported as part of the Center for Bio-Inspired Energy Science, an Energy Frontier Research Center funded by the US Department of Energy, Office of Science, Basic Energy Sciences under Award DE-SC0000989. Z.W. gratefully acknowledges support from a Ryan Fellowship and the International Institute for Nanotechnology at Northwestern University. We thank J. Kim for useful discussions.

Author contributions

Z.O. and Q.C. designed and performed the experiments and analysed the data on the nanoprism system. Z.W. and E.L. designed the theoretical model and performed the simulations. B.L. performed the experiments on the concave nanocube and nanosphere systems. Z.O., Z.W., E.L. and Q.C. wrote the manuscript.

Competing interests

The authors declare no competing interests.

Additional information

Supplementary information is available for this paper at https://doi.org/10.1038/s41563-019-0514-1.

Correspondence and requests for materials should be addressed to E.L. or Q.C.

Reprints and permissions information is available at www.nature.com/reprints.